Title: Numerical assessment of diffusion-convection-reaction model for the catalytic abatement of phenolic wastewaters in packed-bed reactors under trickling flow conditions

Authors: Rodrigo J.G. Lopes, Rosa M. Quinta-Ferreira

PII: S0098-1354(11)00023-8
DOI: doi:10.1016/j.compchemeng.2011.01.013
Reference: CACE 4183

To appear in: *Computers and Chemical Engineering*

Received date: 17-8-2010
Revised date: 4-1-2011
Accepted date: 9-1-2011

Please cite this article as: Lopes, R. J. G., & Quinta-Ferreira, R. M., Numerical assessment of diffusion-convection-reaction model for the catalytic abatement of phenolic wastewaters in packed-bed reactors under trickling flow conditions, *Computers and Chemical Engineering* (2010), doi:10.1016/j.compchemeng.2011.01.013

Numerical assessment of diffusion-convection-reaction model for the catalytic abatement of phenolic wastewaters in packed-bed reactors under trickling flow conditions

Rodrigo J.G. Lopes and Rosa M. Quinta-Ferreira, *

Centro de Investigação em Engenharia dos Processos Químicos e Produtos da Floresta (CIEPQPF)

GERSE – Group on Environmental, Reaction and Separation Engineering

Department of Chemical Engineering, University of Coimbra

Rua Sílvio Lima, Polo II – Pinhal de Marrocos, 3030-790 Coimbra, Portugal

*Author to whom correspondence should be addressed

Phone: +351-239798723; fax: +351-239798703;

E-mail address: rodrigo@eq.uc.pt

Abstract

Computational Fluid Dynamics (CFD) modeling of trickle-bed reactors with detailed interstitial flow solvers has remained elusive mostly due to the extreme CPU and memory intensive constraints. Here, we developed a comprehensible and scalable CFD model based on the conservative unstructured finite volume methodology to bring new insights from the perspective of catalytic reactor engineering to gas-liquid-solid catalytic wet oxidation. First, the heterogeneous flow constitutive equations of the trickle bed system have been derived by means of diffusion-convection-reaction model coupled within a Volume-of-Fluid framework. The multiphase model was investigated to gain further evidence on how the effect of process variables such as liquid velocity, surface tension and wetting phenomena affect the overall performance of high-pressure trickle-bed reactor. Second, as long as the application of under-relaxation parameters, mesh density, and time stepping strategy play a major role on the final corroboration, several computational runs on the detoxification of liquid pollutants were validated accordingly and evaluated in terms of convergence and stability criteria. Finally, the analysis of spatial mappings for the reaction properties enables us to identify the existence of relevant dry zones and unveil the channeling phenomena within in the trickle-bed reactor.

Keywords: Computational fluid dynamics; Trickle-bed Reactor; Multiphase flow; Catalytic Wet Oxidation; Total Organic Carbon; Temperature

1. Introduction

Trickle-bed reactors are employed in many engineering applications that go from hydrotreatments and hydrocracking reactions in the petrochemical processing industries to the environmental detoxification of exhaust gases and polluted wastewaters from chemical plants, among numerous others. In the realm of environmental reaction engineering, trickle beds are envisaged as an effective route capable of destroying the water-dissolved biorefractory pollutants (Bhargava, Tardio, Prasad, Foger, Akolekar, & Grocott, 2006) by means of catalytic wet oxidation (CWO). In this regard, numerical simulations have received an increasing awareness within the industry and research communities to better understand the operation of TBRs. Multiphase CFD codes are then expected to play an even bigger role on the ubiquitous intensification of resources to reinforce simultaneously and virtually prevent organic and inorganic wastes emissions.

The design of trickle beds is often considered as a cumbersome task since one of the critical parameters that dominate the multiphase flow phenomena is the multicomponent diffusion plus the highly nonlinear chemical kinetics. For catalytic wet oxidations, the complexity can even be increased depending on the hydrodynamic flow regime in which the trickle bed is to be operated. Under trickling flow conditions, the residence time should obey specific criteria such that no catalyst is wasted and concomitantly the remediation of liquid pollutants is almost complete. In practice, the operation and design of TBRs is adjusted to near-optimum by stacking together the above-mentioned facts concerning further industrial application of CWO. This task calls not only for the total mineralization of liquid pollutants but also for the secure and stable operations without prematurely deactivate the catalyst.

The low interaction regime achieved under trickling flow conditions is described by low Peclet number and the pollutant diffusion transport cannot be neglected in such circumstances. The diffusion of liquid-dissolved contaminants in a multi-component system is

dictated not only by its own concentration gradient but also by the concentration gradient of the other species in the system conversely to what happens in binary pollutant systems. The multiphase flow governing equations for such a system are coupled and nonlinear second-order elliptic partial differential equations. The degree of coupling allows us to solve numerically those equations either in a segregated or non-segregated fashion. As a rule of thumb for concentrated multicomponent mixtures, segregation of the governing equations cannot be performed directly so the numerical strategy is performed by under-relaxation parameters to produce the system of equations amenable to numerical solution. On the contrary, in case of dilute mixtures there exists an opportunity to use a reference pollutant which constitutes most of the mixture and these equations become segregated or are only weakly coupled. In case of segregated frameworks, the self-diffusion operator is computed implicitly, while the diffusion due to the other pollutant species is treated explicitly. This fact results in an iterative algorithm whose convergence depends on the strategy used to conserve the overall mass constitutive equation.

In this work, the multiphase flow governing equations for a trickle-bed reactor will be assessed on how the convergence criterion for the mass fraction balance can be imposed explicitly, and if the transport properties are not held constant, the convergence of this semi-implicit system of equations requires under-relaxation even for one-dimensional calculations. Unless stated otherwise, our case-study comprises a multi-dimensional formulation, where the spatial operators have to be additionally split to enable use of iterative algorithm so the convergence will be guaranteed with optimum under-relaxation parameters since it is dependent on the computational mesh aperture. On the prevention of the decoupling of pressure and velocity variables in three-dimensional grids, the numerical approximation of advective terms can give rise to false diffusion errors. This fact can be avoided if one chooses flux discretization schemes that should eliminate the cross-wind error without sacrificing the

scheme stability. In addition to this requirement to suppress oscillations of velocity and pressure without accuracy deterioration, there is also the reinforcement of divergence-free constraint condition for the velocity field in the simulation of incompressible Navier-Stokes equations. A straightforward implementation to comply with mass conservation is to apply the mixed formulation for solving the multiphase flow equations subjugated by the incompressible constraint condition. A major drawback of this approach is the conception of a less diagonally dominant coupled system of equations. The computation of primitive variables is then affected by the poor eigenvalue distribution and the increased sized of the resulting matrix. In this ambit, the segregated algorithm can be applied to circumvent the numerical issues that characterize the mixed formulation so the pressure scalar field (Poisson equation) is obtained independently from the velocity vector field by the solution of the momentum balance equation.

The present article is divided into three major parts: first, a brief literature survey is presented on specific cases to solve the advection-diffusion-reaction equation. Afterwards, the multiphase flow governing equations for a TBR under reactive flow conditions are detailed with the computational methodology used in the simulation procedure followed by the simulation setup and the relevant boundary conditions. Proceeding further, results are presented encompassing qualitative and quantitative comparisons of computed and experimental total organic carbon (TOC) concentration and temperature profiles. Convergence plots are discussed for several under-relaxation factors and various mesh sizes as well as different time steps. Finally, representative interstitial reaction flow maps of TOC and thermal silhouettes will be analyzed by three-dimensional computational mappings.

2. Previous work

Hassanzadeh, Abedi, & Pooladi-Darvish (2009) have presented a comparative study of flux-limiting methods for numerical simulation of gas–solid reactions with Arrhenius type reaction kinetics. Mainly motivated by the exothermic nature of gas–solid reactions that results in large concentration and temperature gradients, leading to steep reaction fronts, the authors have investigated the application of higher-order and flux-limiting methods for numerically modeling one-dimensional coupled heat and mass transfer accompanied with a heterogeneous gas–solid system. Instead of carrying out fine grid simulations at large scale, which are computationally expensive, or on the other hand, using coarse grid block simulations, which leads to excessive front dissipation/smearing and inaccurate results, they claimed that Superbee, MC, and van Albada-2 flux limiters are superior as compared to other schemes at low grid resolution. Cerbelli, Garofalo & Giona (2008) have evaluated the steady-state performance of an infinitely fast reaction in a three-dimensional open Stokes flow. Different flow protocols were analyzed in terms of the axial behavior of reaction yield as a function of the Peclet number, quantifying the relative importance of convective vs. diffusive transport mechanisms. The authors have come to the conclusion that the transformation of the standard eigenvalue–eigenfunction formulation into a generalized form could greatly improve the rational design of geometry and operating conditions of micro and ordinary lengthscale continuous reactors operating under laminar flow conditions. Li & Christofides (2008) have developed two approaches for an optimal control methodology of diffusion-convection-reaction processes using reduced-order models. Whereas in the first approach, the partial differential equation is first discretized in space and time using the finite difference method written in the form of a discrete-time state-space model with sparse state, input and output matrices, the second approach is characterized by the continuous-time finite-dimensional state-space model which is constructed directly from the partial differential equation through application of orthogonal collocation on finite elements in the spatial domain. These different

frameworks were applied successfully to a diffusion-convection process and a diffusion-convection-reaction process. Alhumaizi, Henda & Soliman (2003) have analyzed numerically the behavior of a homogeneous tubular reactor in which a cubic autocatalytic reaction is coupled to diffusion and convection transport. They have applied essentially non oscillatory and total variation diminishing finite difference methods and found these high-resolution schemes critical to computed efficiently sharp moving fronts exhibited by the strongly convective problems. Later, Alhumaizi (2004) has discussed comparatively different finite difference methods for the numerical simulation of reacting flow to solve a one-dimensional convection-reaction problem. It was found that high-resolution techniques such as flux-corrected transport, the monotone upstream scheme for conservation laws and weighted essentially non-oscillatory schemes are efficient to track steep moving fronts and are essential for cases which use small numbers of grid points in comparison with the traditional first- or second-order difference schemes. Zalc & Muzzio (1999) simulated parallel-competitive reactions in a two-dimensional chaotic flow. The time evolution and spatial distribution of species concentration were found to depend strongly both on the nature of the flow and on the relative rates of the two reactions under three different flow conditions. The authors claimed that significant spatial heterogeneity exists throughout the duration of the reactive mixing simulation even in the globally chaotic flow for those types of diffusion-convection-reaction systems.

The aforementioned survey revealed that CFD models can be trustfully applied in different frameworks; nevertheless such approach has scarcely been reported to predict the reaction behavior of trickle beds by means of diffusion-convection-reaction models. Here, we investigate a Volume-of-Fluid model to gain further evidence on how the effect of process variables such as liquid velocity, surface tension and wetting phenomena affect the overall performance of high-pressure trickle-bed reactor. A Volume-of-Fluid model was developed to

simulate the multiphase reactive flow on the catalytic wet oxidation of mimicked phenolic wastewaters. As long as the mesh density, time stepping strategy and the application of under-relaxation parameters play a major role on the final corroboration of the multiphase model, several computational runs on the detoxification of liquid pollutants have to be validated accordingly and performed at transient conditions to realize new reactive flow insights of multiphase flow environment.

3. Mathematical Model

3.1. Governing Flow Equations

A trickle bed based on a cylindrical geometry (50 mm_{ID}×1.0 m_{Length}) was modeled with a specified void fraction and a set of fluid physical properties. The computational geometry was designed so that a distance gap of about 3% of the sphere diameter facilitate the grid generation avoiding numerical difficulties that arise in the calculation of convective terms as described elsewhere (Lopes & Quinta-Ferreira, 2008; Nijemeisland & Dixon, 2001). The VOF method was used to compute velocity field, liquid volume fraction distributions as well as the total organic carbon concentration that was used to quantify the mineralization degree of liquid pollutants. The multiphase flow is assumed to be vertical downward and incompressible, with the mathematical description for the flow of a viscous fluid through a three dimensional catalytic bed based on the Navier-Stokes equations for momentum and mass conservation. The variable fields are shared by both phases and correspond to volume-averaged values knowing the volume fraction, α_q, of each phase, q, in the entire computational domain. The volume fraction equation for the phase q is given by:

$$\frac{\partial}{\partial t}\left(\alpha_q \rho_q\right) + \nabla \cdot \left(\alpha_q \rho_q \mathbf{U}_q\right) = 0 \quad \text{with } q = g \text{ or } l \tag{1}$$

where g and l denote, respectively, the gas and liquid phases, t, being the time, and through the resolution of the momentum equation shared by the two considered fluids:

$$\frac{\partial}{\partial t}\left(\alpha_q \rho_q \mathbf{U}_q\right) + \nabla \cdot \left(\alpha_q \rho_q \mathbf{U}_q \mathbf{U}_q\right) = -\alpha_q \nabla p + \alpha_q \rho_q \mathbf{g} + \nabla \cdot \alpha_q \left(\overline{\overline{\tau}}_q + \overline{\overline{\tau}}_{t,q}\right) + \mathbf{I}_q \quad \text{with } q = g \text{ or } l \tag{2}$$

where p, $\mathbf{g}$ and the physical properties (density, ρ; and viscosity, μ) being determined by volume-weighted averages. $\mathbf{I}_q$ is the interphase momentum exchange term and $\overline{\overline{\tau}}_q$ and $\overline{\overline{\tau}}_{t,q}$ are, respectively, the viscous stress tensor and the turbulent stress tensor, defined as follows:

$$\overline{\overline{\tau}}_q = \mu_q \left(\nabla \mathbf{U}_q + \nabla \mathbf{U}_q^t\right) + \left(\lambda_q - \frac{2}{3}\mu_q\right) \nabla \mathbf{U}_q \overline{\overline{I}} \tag{3}$$

and

$$\overline{\overline{\tau}}_{t,q} = \mu_{t,q} \left(\nabla \mathbf{U}_q + \nabla \mathbf{U}_q^t\right) - \frac{2}{3}\left(k_q + \mu_{t,q} \nabla \mathbf{U}_q\right) \overline{\overline{I}} \tag{4}$$

3.2. Free Surface Model: Surface Tension and Wall Adhesion

The continuum surface force model has been used to compute the surface tension (Brackbill, Kothe, & Zemach, 1992). The pressure drop across the surface depends upon the surface tension coefficient, σ, and the surface curvature as measured by two radii in orthogonal directions, R_1 and R_2, as expressed by Eq. 5.

$$p_2 - p_1 = \sigma \left(\frac{1}{R_1} + \frac{1}{R_2}\right) \tag{5}$$

where p_1 and p_2 are the pressures in the two fluids on either side of the interface. The surface curvature is computed from local gradients in the surface normal at the interface. n is the surface normal, defined as the gradient of α_i : $n = \nabla \alpha_i$. The curvature, κ , is defined in terms of the divergence of the unit normal, $\hat{n}$: $\kappa = \nabla \cdot \hat{n}$ where $\hat{n} = \frac{n}{|n|}$. The forces at the surface are expressed as a volume force using the divergence theorem assuming the form of Eq. 6.

$$F_j = \sum_{\text{pairs } ij,\, i<j} \sigma_{ij} \frac{\alpha_i \rho_i \kappa_j \nabla \alpha_j + \alpha_j \rho_j \kappa_i \nabla \alpha_i}{\frac{1}{2}\left(\rho_i + \rho_j\right)} \tag{6}$$

3.3. Species Continuity and Energy Equations

The predicted flow field including velocities and volume fractions of both phases was further used for solving species transport equations for simulating the catalytic wet air oxidation of a model phenolic solution in the trickle-bed reactor. These equations are expressed in the mass balance equation for any species, *i*:

$$\frac{\partial \alpha_q \rho_q C_{q,i}}{\partial t} + \nabla \cdot \left(\alpha_q \rho_q u_q C_{q,i}\right) = \nabla \cdot \left(\alpha_q \rho_q D_{i,m} \nabla C_{q,i}\right) + \alpha_q \rho_q S_{q,i} \quad (7)$$

where, $C_{q,i}$ is the concentration of species i in the q^{th} phase (gas or liquid), ρ_q and α_q is the density and volume fraction of the q^{th} phase. $S_{q,i}$ is the source for species i in phase q. Volume averaged properties of fluids were used for calculating the flux across the control cell. Two-film theory was used for accounting mass transfer and the resistance in gas-liquid film was considered as the rate limiting resistance (Bhaskar, Valavarasu, Sairam, Balaraman, & Balu 2004). Mass transfer coefficient was computed according to the Satterfield et al. correlation and heat transfer coefficient was calculated according to the literature correlation as expressed by equations 8 and 9, respectively (Satterfield, van Eek, & Bliss, 1978; Boelhouwer, Piepers, & Drinkenburg, 2001).

$$Sh = 0.815\, Re^{0.822}\, Sc^{1/3} \quad (8)$$

$$Nu = 0.111\, Re^{0.8}\, Pr^{1/3} \quad (9)$$

The energy equation, also shared among the phases, is shown in equation 10:

$$\frac{\partial}{\partial t}\left(\rho E\right) + \nabla \cdot \left(\vec{v}\left(\rho E + p\right)\right) = \nabla \cdot \left(k_{eff} \nabla T\right) + S_h \quad (10)$$

The VOF model treats energy, *E*, and temperature, *T*, as mass-averaged variables:

$$E = \frac{\sum_{q=1}^{n} \alpha_q \rho_q E_q}{\sum_{q=1}^{n} \alpha_q \rho_q} \quad (11)$$

where E_q for each phase is based on the specific heat of that phase and the shared temperature. The properties ρ and k_{eff} (effective thermal conductivity) are shared by the phases. The source term, S_h, contains contributions from volumetric reaction heat sources, which is given by the product $\Delta H \times \rho \times r_{TOC}$.

3.4. Two-phase k-ε turbulence model

Taking into account that the Reynolds numbers range for the gas phase is wide (min: 10, max: 2500), the mixture *k-ε* approach is used for turbulence. For incompressible flows, the turbulence parameters are calculated from equations 10-11:

$$\frac{\partial}{\partial t}(\rho_m k) + \nabla \cdot (\rho_m \vec{u}_m k) = \nabla \cdot \left(\frac{\mu_{t,m}}{\sigma_k} \nabla k \right) + G_{k,m} - \rho_m \varepsilon \tag{12}$$

$$\frac{\partial}{\partial t}(\rho_m \varepsilon) + \nabla \cdot (\rho_m \vec{u}_m \varepsilon) = \nabla \cdot \left(\frac{\mu_{t,m}}{\sigma_\varepsilon} \nabla \varepsilon \right) + \frac{\varepsilon_m}{k_m} \times (C_{1\varepsilon} G_{k,m} - C_{2\varepsilon} \rho_m \varepsilon) \tag{13}$$

and the turbulent viscosity $\mu_{t,m}$ and the production of turbulence kinetic energy, $G_{k,m}$ are computed from Eq. 14.

$$\mu_{t,q} = \rho_q C_\mu \frac{k_q^2}{\varepsilon_q}$$

$$G_{k,m} = \mu_{t,m} \left(\nabla \vec{u}_m + (\nabla \vec{u}_m)^T \right) : \nabla \vec{u}_m \tag{14}$$

C_μ is equal to 0.09 and $C_{1\varepsilon}$ and $C_{2\varepsilon}$ are the constants of standard *k-ε* model: 1.44 and 1.92, respectively, whereas σ_k and σ_ε are the turbulent Prandtl numbers for *k* and *ε*, 1.0 and 1.3, respectively.

3.5. Numerical simulation

The interstitial space of the trickle-bed reactor was designed through a tetrahedral mesh representing that was created using the integrated solid modeling and meshing program

GAMBIT mimicking the characteristic dimensions of commercial catalyst N-140 supplied by the Süd-Chemie Group, Munich. The VOF method simulates free-surface flow by means of a fluid fraction function, which has a value between unity and zero. The discretization of the governing equations is done by the finite-volume method. The grid independency was established after the evaluation of different mesh natures and apertures in order to isolate mesh related discretization errors. All transport equations were discretized to be at least second order accurate in space. A segregated implicit solver available in commercial CFD package FLUENT 6 was employed to evaluate the resulting linear system of equations. The conditions required for grid convergent results are based on a 1% relative error criterion and the simulations accuracy has been assessed by comparisons to experimental data available in the literature. At the interface, the additional interaction conditions depend on interfacial velocity and gradient of the surface tension.

The CWAO kinetic parameters for the commercial catalyst N-140 were similarly derived to the work developed by Lopes, Silva & Quinta-Ferreira (2007). The right-hand side term of Eq. 7, $S_{i,q}$, include the reaction rates in terms of the total organic carbon concentration of the lumped species *A*, *B* and *C* as represented by Eq. 15:

$$-r_{TOC_A} = -\frac{d\,C_{TOC_A}}{dt} = \left(k_1' + k_2'\right) C_{TOC_A}$$
$$-r_{TOC_B} = -\frac{d\,C_{TOC_B}}{dt} = k_3' C_{TOC_B} - k_2' C_{TOC_A} \qquad (15)$$

where first order reactions were assumed for each mechanism step of the Generalized Kinetic Model. After integrating these equations a mathematical expression for TOC evolution is obtained in Eq 16:

$$\frac{C_{TOC}}{C_{TOC_0}} = \frac{k_2'}{k_1' + k_2' - k_3'} e^{-k_3' t} + \frac{k_1' - k_3'}{k_1' + k_2' - k_3'} e^{-\left(k_1' + k_2'\right) t} \qquad (16)$$

The activation energies and the pre-exponential factors were calculated by using the Arrhenius plot for the N-140 kinetic studies. These values were used in the corresponding expressions of the reaction rate constants k'_1, k'_2, k'_3 as a function of temperature, according to Arrhenius law as described in Eq 17:

$$k_1^{'} = 452 \cdot \exp\left(-\frac{3.121\times10^3}{T}\right) \min^{-1};$$
$$k_2^{'} = 28.1 \cdot \exp\left(-\frac{3.612\times10^3}{T}\right) \min^{-1}; \quad (17)$$
$$k_3^{'} = 4.32\times10^6 \cdot \exp\left(-\frac{9.814\times10^3}{T}\right) \min^{-1}$$

The inlet turbulence quantities such as turbulent kinetic energy and turbulent dissipation rate were specified based on FLUENT documentation. The turbulent kinetic energy (k) was estimated from turbulence intensity as expressed in Eq. (18).

$$k = \frac{3}{2}(uI)^2 \quad (18)$$

where I is the turbulence intensity being given by Eq. 19.

$$I = 0.16\left(\mathrm{Re}_{d_H}\right)^{-1/8} \quad (19)$$

The turbulent dissipation rate (ε) was estimated from the turbulent viscosity ratio as expressed by Eq. (20).

$$\varepsilon = \rho C_\mu \frac{k^2}{\mu}\left(\frac{\mu_t}{\mu}\right)^{-1} \quad (20)$$

where C_μ is an empirical constant specified in the turbulence model (0.09). At 30 *bar* and 200 ^oC, the inlet turbulent kinetic energy for the liquid (u_L = 0.0055 m/s) and gas phase (u_G = 0.020 m/s) was 0.518 and 8.117 mm^2/s^2, respectively, whereas the turbulent dissipation rate was 0.0654 and 2.934 mm^2/s^3.

Initial and boundary conditions for the gas and liquid phases are systematized by Table 1, whereas the relevant gas and liquid thermophysical properties at P=30 bar used in the VOF simulations are summarized in Table 2. At the outflow boundary no user defined boundary conditions for species are necessary and the zero diffusive flux was applied in the species transport equation. In Eq. 10, S_h includes sources of enthalpy due to chemical reaction of phenolic compounds: -3000 kJ/mol. Water properties, dissolved oxygen, phenolic compound diffusion coefficients, water and gas heat capacities, water heat of evaporation, heats of reaction, water vapour pressure and water density have been obtained from data or methods included in Reid, Prausnitz, & Poling (1987). Henry constants for oxygen solubility in water are taken from Himmelblau (1960). Phenolic compound and oxygen molecular diffusion coefficients have been also estimated by the methods of Wilke & Chang (1955) and Siddiqi & Lucas (1986). Effective diffusion coefficient of pollutant in water and gaseous oxygen and solid mass transfer coefficient have been estimated from Piché, Larachi, Iliuta, & Grandjean (2002). Phenolic compound liquid – solid mass transfer coefficient has been calculated from Goto & Smith (1975) and gaseous oxygen – liquid volumetric mass transfer coefficient has been derived from Iliuta, Larachi, Grandjean, & Wild (1999).

Computations are time dependent and were performed until steady state conditions were reached. Standard wall functions were employed for turbulent flow conditions. Table 3 shows the minimum and maximum values obtained for the y^+ parameter around the particle surface for the different Reynolds numbers. The literature studies in turbulence modeling and near-wall treatment have indicated that values of $20<y^+<100$ allow the use of a standard wall function, and values of $1<y^+<10$ allow the use of a two-layer modeling scheme. Indeed, values of y^+ in the particle surface for the selected meshes were in the range of $0.01<y^+<200$. Notwithstanding these values make these meshes inappropriate for using an standard wall function, except for the cases at low Reynolds, FLUENT solver allows the range for wall

function to start on values of y^+=30-50, which were typically the most common dimensionless wall distance value (y^+) for the particle surface under different Reynolds numbers.

The multiphase reactor in our trickle bed pilot plant comprises a cylindrical geometry with the following dimensions 50 mm of internal diameter and 1.0 m length and the experimental procedure has been described elsewhere (Lopes & Quinta-Ferreira, 2010).. Having previously considered that the trickle-bed reactor was filled with 10 layers in which around 200 nonoverlapping spherical particles of 2-mm diameter were necessary for each axial layer, we had made use of parallel computing on 48 nodes to deal with high memory requirements that were necessary to cope with a single computing node. Here, the three dimensional simulations have been carried out on Linux cluster based on AMD64 Dual-Core 2.2 GHz processor. As a single node is concerned with 20 mm of computational domain, the remainder of the calculations has been carried out simultaneously on 47 nodes. This computed methodology enable us to operate on the principle that large chemical reaction engineering problems can be divided into smaller ones, which are then solved concurrently to mimic the factual dimensions of the experimental installation.

4. Results and discussion

4.1. Computational grid aperture

The numerical accuracy of every finite volume solution has been assessed to certain extent on the selection of appropriate computational meshes. We performed several computational runs to figure out the optimum mesh density, generating converged solutions by means of successive mesh refinements. The procedure roughly consists on the parametric optimization querying the effect of different differencing schemes on the momentum and volume fraction balance equation. High-order differencing schemes based on Compressive Interface Capturing Scheme for Arbitrary Meshes (CICSAM) and High Resolution Interface Capturing (HRIC)

schemes were found to agree better with the experimental data from the literature given that its formulation includes inherently the minimization of artificial numerical dissipation as described elsewhere (Lopes & Quinta-Ferreira, 2009). The computational grid is first refined in the flow direction to duplicate the total number of volumes that were present in the parent mesh. No deviations are found in concentration and temperature profiles compared to those obtained before the mesh refinement.

The refinement is performed in eight levels: four levels for the coarser meshes with 2×10^5, 6×10^5, 1×10^6, 1.4×10^6 of tetrahedral cells and four levels for the finer meshes with 1.8×10^6, 2.2×10^6, 2.6×10^6 and 3×10^6 of tetrahedral cells. Figure 1 displays the influence of the number of tetrahedral cells on the total organic carbon concentration profile when the catalytic abatement of phenolic wastewaters was simulated at L=6 kg/m^{2}s, G=0.3 kg/m^{2}s and T=200 ºC, P=30 bar. As can be seen from Fig. 1, the increase of mesh density led to an asymptotic solution as one increases the number of cells from 2.2×10^6 onwards. Low mesh density characterized by 2×10^5 of tetrahedral cells at particle surface led to erroneous solutions due to an incorrect definition of boundary layer. As long as the mesh density increases, the theoretical predictions of total organic carbon conversion improve noticeably. When the mesh is successively refined to give ca. tenfold the number of cells, the same performance is repeated confirming that the solutions obtained with the higher densities meaning that were already converged. However, a significant rise in computational time is reported which for the densest mesh is several hours. Depending on the hydrodynamic flow regime, the boundary conditions needed to enforce along the whole boundary or parts of the boundary enclosing the computational domain may be different for the numerical solution of governing differential equations. This is partly ascribed to the low interaction regime achieved between the gas and the liquid phase under trickling flow conditions. Here, it is anticipated for pulsing flow simulations that those boundary conditions emerge differently from the physics underlying

the process. However, for the current results, the simulated variations of the field unknowns are not found to be perfectly symmetrical along the axis of domain parallel to the direction of flow. This fact may be attributed to the geometric constraints that characterized the packed bed flow.

In order to properly capture the boundary layer now on the temperature profile and regarding also the mesh sensitivity analysis, several computational runs were additionally performed changing the mesh density on the catalyst particle surface. The effect of mesh aperture on the thermal behavior of the trickle-bed reactor is portrayed in Fig. 2 at L=6 kg/m^{2}s, G=0.3 kg/m^{2}s and T=200 ºC, P=30 bar. Once again, the CFD predictions converged as soon as we used a computational grid comprising 2.2 million of tetrahedral cells. There is also an interesting fact revealed by Figs. 1 and 2, which is related to the monotony exhibited by the total organic carbon conversion and temperature profiles. As evidenced by the mesh sensitivity analysis, the asymptotic behavior of total organic carbon profile is monotonically increasing until the final conversion approaches the experimental value at steady-state. Likewise, the temperature profile is a monotonically increasing function as one increases the density of the computational grid. As long as the catalytic wet oxidation follows the Arrhenius's law, the higher conversions are accompanied with increasing values of the bulk phase temperature as exhibited by thermal profile in Fig. 2.

4.2. Time step sensitivity tests

With the provision that the reaction kinetics of catalytic wet oxidation is non-linear, it posed additional constraints on the selection of the iterative procedures for the solution of the algebraic equations derived from the finite volume formulation. In order to cope with this complexity arising from the numerical analysis, the intrinsic rate of reaction is often expressed in terms of the catalyst activity which is quite justifiable on the basis that the

commercial catalyst is virtually non-porous which promotes the surface reactions. The constitutive equations are in macroscopic form applicable to the geometric scale of reactor, and conversely the catalytic wet oxidation kinetics is expressed in a microscopic form in terms of active sites present on the catalyst surface to promote additional suitability. Since one of the aims of this research was to further unveil the influence of surface reaction on multiphase fluid flow and gas-liquid distribution as well as heat/mass transport phenomena, one should bear in mind that the equation form of catalytic wet oxidation kinetics may vary depending on the level of hydrodynamic interaction regime.

Similarly, the stability of finite volume solutions depends on the type of the time-stepping scheme employed for the temporal discretization of the constitutive equations. During the CFD multiphase calculations, we employed first-order and second-order time discretization methods. This latter scheme was found to give confident computed results in comparison to the former one as long as the second-order time-accurate scheme achieves its accuracy by using an Euler backward approximation in time. This fact can in all likelihood be ascribed to the fully implicit methodology which highlighted an unconditional stability. A fair implementation of one of these methods for solving the scalar transport equation entails more than the time-stepping formula. Additionally, we have investigated the time step in the range: 10^{-5}, 10^{-4}, 10^{-3} and 10^{-2} s. Figure 3 plots the CFD computations of total organic carbon conversions attained with those values at L=6 kg/m^{2}s, G=0.3 kg/m^{2}s and T=200 ºC, P=30 bar. A similar asymptotic trend was depicted in Fig. 3 so we have identified a time step of 10^{-5} s which agreed better with the experimental data. Concomitantly, the analysis of the temperature profile obtained at L=6 kg/m^{2}s, G=0.3 kg/m^{2}s and T=200 ºC, P=30 bar reinforced the above-mentioned selection on the time step assessment, see Fig. 4. Once again, it is worth remarking the analogous behavior that described the total organic carbon conversion and temperature profiles illustrated in Figs. 3 and 4. The Arrhenius's temperature dependence of

the rate constant for the catalytic wet oxidation is emphasizing hitherto on the monotonic nature of mesh density and time step profiles.

4.3. Convergence and stability

As with any other type of CFD codes based on finite volume solution method, one should bear in mind that convergence and stability criteria should be investigated to obtain CFD independent results with respect to validation and verification activities. Having examined the effect of several mesh apertures and different time steps on the reaction properties, here we analyze the temporal evolution of the computed residuals in convergence plots. The above-mentioned workflow was dictated by the application requirement of different under-relaxation parameters and by the geometry details of our computational grid so the tetrahedral mesh of the catalytic bed was typically characterized with around 443 spherical particles of 2 mm diameter for each axial layer. If one uses 2.2×10^{6} computational nodes for each layer, we needed approximately 3.01×10^{8} nodes to obtain an asymptotic solution. As there are typically 9 unknowns at each node comprising 4 mass fractions, temperature, pressure, and 3 velocity components, the CFD calculations were performed with ca. 2.71×10^{9} unknowns.

The convergence plot obtained for various under-relaxation factors using segregated solution on the calculation of total organic carbon conversion is shown in Fig. 5 at L=6 kg/m^{2}s, G=0.3 kg/m^{2}s and T=200 ºC, P=30 bar. The accuracy and convergence of the model was investigated with 3 different under-relaxation factors: 0.6, 0.7, 0.8. It was concluded that the application of the middle value for the computation of TOC conversion with finite volume space discretization could not be very effective when dealing with complicate geometries and physical properties variations. The numerical simulation was found to be reliable with both extreme values to investigate the effects of geometric and hydrodynamic parameters on the mineralization degree of liquid pollutants by catalytic wet oxidation. Figure 6 illustrates the

application effect of different under-relaxation factor on the computation of the temperature variable at L=6 kg/m^{2}s, G=0.3 kg/m^{2}s and T=200 ºC, P=30 bar. The qualitative behavior exhibited by Figs. 5 and 6 is connected with the difference obtained with under-relaxation factor of 0.8 for the temperature, which required a prohibitive number of iterations to achieve the convergence criterion. Whereas this factor is almost kept to the matching value in that range to give confident predictions on the TOC conversion, extensive timing studies was not feasible for such an under-relaxation factor on the calculation of temperature profiles.

Figure 7 shows the convergence plot of total organic carbon conversion for three different mesh sizes: 1.8×10^6, 2.2×10^6, 2.6×10^6 at L=6 kg/m^{2}s, G=0.3 kg/m^{2}s and T=200 ºC, P=30 bar, whereas the convergence plot of temperature is depicted by Fig. 8 for the same computational grid densities. As can be seen from both convergence profiles, the results have exhibited numerical fluctuations in the first 20000 iterations so to circumvent these oscillations high-resolution discretization algorithm based on the monotone upstream scheme for conservation laws was found to be computationally efficient and tractable. Generally, the average oxidation of liquid pollutants decreased prominently with increasing flow rates of the effluent feed stream under convection dominated flow conditions. The simulated results were in good agreement with the experimental data and the comparison suggested that the transport phenomena in the trickle-bed reactor can be reliably predicted and easily understood compared to macroscopic reactor systems. However, the simulations are not insensitive in analyzing the reaction conversion and bulk temperature for different numerical tuning parameters as demonstrated by the influence of under-relaxation factors and mesh apertures, see Figs. 5-6 and 7-8, respectively. The numerical solution of the constitutive equations was stiff in temporal direction due to diffusive terms and steep in spatial direction due to convective terms. To better underline this behavior, it can be advanced that non-oscillatory and total variation diminishing methods improve remarkably the accuracy eliminating the

oscillations at the expense of increased computational costs. As mentioned before, our case-study encompassed a trickle bed operated under low interaction regimes; nevertheless the energy and species concentration balances are convection-diffusion equations that may require special treatment to avoid spurious oscillations in the simulated results under pulsing flow conditions. This is somewhat related with the advection level which is the dominating transport mechanism for chemical species and heat/mass transfer phenomena for such operating hydrodynamic regimes.

The convergence plots of total organic carbon conversion and temperature is illustrated in Figs. 9 and 10, respectively, for different time steps in the range: 10^{-5}, 10^{-4}, 10^{-3} s at L=6 kg/m^{2}s, G=0.3 kg/m^{2}s and T=200 ºC, P=30 bar. This numerical solution parameter has been found to disclose new computational findings as can be seen from both reactive flow properties. As already discussed on the advection term, an improper choice of time stepping scheme may lead to unstable and oscillatory results and higher order time-stepping schemes were required. Indeed, as one can observe in Figs. 9 and 10 no oscillations were detected in the results confirming that convection was not the principle mode for the transport of gas oxidant and liquid pollutants as well as energy in the present case. Since, the mass transport was not found to be dominated by convection; the total organic carbon concentration needed more reactor length to attain steady state mineralization level. On the contrary, concentration of carbon dioxide was almost negligible in the first half of the reactor so the maximum respective concentration was observed near the catalyst.

4.4. Reaction flow maps

For the present case-study, catalytic wet oxidation of phenolic wastewaters was chosen as the candidate system to evaluate the reaction map of interstitial flow fields mainly because it is processed within the trickle-bed reactor. As this sort of multiphase reactor can play a major

role in the realm of environmental lifecycle analysis, its design is often dictated by fundamental criteria for the efficient design which encompass the identification and characterization of hydrodynamics such as phase holdup, pressure drop, and liquid distribution. To enable the analysis of spatial mappings of reaction properties, we investigated computationally the interstitial flow in the current environmentally-based trickle-bed reactor given the inherent difficulties of conventional measurement methods which mainly confer a global view on the trickle bed performance.

Figure 11 shows a semi-cylindrical slice made inside the catalytic bed at L=6 kg/m^{2}s, G=0.3 kg/m^{2}s, P=30 bar, T=200ºC illustrating an instantaneous snapshot of liquid phase distribution colored by total organic carbon concentration, while Fig. 12 shows the same the Instantaneous snapshot of liquid phase distribution colored by liquid temperature. These three-dimensional visualizations of trickle flow shows two distinct regions of liquid holdup: liquid rivulets characterized by their relatively large cross-sectional area and surface liquid seen as thin layers on the solid surfaces. In this ambit, the rivulet formation has been identified experimentally by means of magnetic resonance imaging (Gladden, Lim, Mantle, Sederman, & Stitt, 2003). Moreover, computer-assisted tomography [32,33] has been used to categorize the rivulet/film taxonomy in multiphase gas-liquid distribution studies. The Courant number distribution maps showed that the *Courant-Friedrichs-Lewy* condition was always met during the CFD simulations. This computational domain is located in the TBR center so that it can be assumed that inlet flow effects can be neglected throughout the entire reactive flow simulations. Under high-pressure operating conditions, the computed isosurfaces depicted in Figs. 12 and 13 revealed spatially the existence of relevant dry zones formed in the packed bed and unveil the channeling phenomena typically encountered in lower interaction regimes that is often identified as the main cause of poor hydrodynamic and reaction performance of trickle-bed reactors.

5. Conclusions

State-of-the-art CFD simulation codes can be used to unveil new perspectives into the heterogeneous multiphase flow of trickle beds. In this realm, a CFD model based on the conservative unstructured finite volume methodology has been proposed to investigate in detail the interstitial reactive flow. The catalytic wet oxidation of mimicked phenolic pollutants has served as our case-study to gain further evidence on the application of under-relaxation parameters, mesh density, and time stepping strategy play a major role on the final corroboration. The segregated solver has been found to reveal good properties in terms of convergence and stability criteria, which enabled the further corroboration. The diffusion-convection-reaction model coupled within a VOF model gave rise to different catalyst wetting levels under trickling flow conditions. It also highlighted the inhomogeneous reactive flow environment within the trickle-bed reactor and can be further exploited on the simulation of complex multiphase flows with adjustable parameters.

Acknowledgment

The authors gratefully acknowledged the financial support of *Fundação para a Ciência e Tecnologia*, Portugal.

Nomenclature

$C_{\mu}, C_{1\varepsilon}, C_{2\varepsilon}$	k-ε model parameters: 0.09, 1.44, 1.92
C	Specie concentration, ppm
c_p	Specific heat, J/(kg K)
D	Mass diffusivity, $m^2.s^{-1}$
d_p	Catalyst particle nominal diameter, m
E	Thermal energy, J
$\vec{g}$	Gravitational acceleration, $9.81 m/s^2$
G	Gas mass flux, kg/m^2s
G_{kL}	Generation rate of turbulent kinetic energy

h	Convective heat transfer coefficient, W/(m^{2}K)
$\mathbf{I}_q$	Interphase momentum exchange term
k	k-ε model kinetic energy
K	Mass transfer coefficient, m.s^{-1}
k_f	Thermal conductivity, W/(m K)
k_{eff}	Effective thermal conductivity, W/(m K)
l	Characteristic length, m
L	Liquid mass flux, kg/m^{2}s
$\hat{n}_w$	Unit vector normal to the wall
Nu	Nusselt number [hl/k_f], dimensionless
p	*P*ressure, bar
Pr	Prandtl number [$C_p\mu/k_f$], dimensionless
$-r$	Oxidation rate *(mg/L)×(1/min)*
Re_q	Reynolds number of q^{th} phase [$(\rho_q u_q d_p/\mu_q$], dimensionless
S_i	Source mass for phase i, ppm
Sh	Sherwood number [Kl/D], dimensionless
S_h	Source term containing volumetric reaction heat, J
t	Time, s
$\hat{t}_w$	Unit vector tangential to the wall
T	Temperature, *K*
TOC	Total organic carbon, ppm
$\vec{u}$	Superficial vector velocity, m/s
z	Axial coordinate, m
Greek letters	
α_i	Volume fraction of i^{th} phase
ε	k-ε model dissipation energy
κ	Gas-liquid interface curvature
ρ_q	Density of q^{th} phase, kg/m^3
Δp	Total pressure drop, Pa
σ	Surface tension coefficient,
σ_k , σ_ε	k-ε model parameters: 1.2, 1.0
τ	Residence time, s

1	$\overline{\overline{\tau}}_q$	Viscous stress tensor of q^{th} phase, Pa
2	$\overline{\overline{\tau}}_{t,q}$	Turbulent stress tensor of q^{th} phase, Pa
3	θ_w	Contact angle at the wall
4	μ_q	Viscosity of q^{th} phase, Pa.s
5		
6	*Subscripts*	
7	*G*	Gas phase
8	*q*	q^{th} phase
9	*L*	Liquid phase
10	*n,m*	Cartesian coordinate direction
11	*S*	Solid phase

References

Alhumaizi, K., Henda, R., & Soliman, M. (2003). Numerical analysis of a reaction-diffusion-convection system. *Computers and Chemical Engineering* 27, 579-594.

Alhumaizi, K. (2004). Comparison of finite difference methods for the numerical simulation of reacting flow. *Computers and Chemical Engineering 28*, 1759-1769.

Bhargava, S. K., Tardio, J., Prasad, J., Foger, K., Akolekar, D. B. & Grocott, S. C. (2006). Wet Oxidation and Catalytic Wet Oxidation. *Industrial and Engineering Chemistry Research 45* (4); 1221-1258.

Bhaskar, M., Valavarasu, G., Sairam, B., Balaraman, K. S., & Balu, K. (2004). Three-Phase Reactor Model to Simulate the Performance of Pilot-Plant and Industrial Trickle-Bed Reactors Sustaining Hydrotreating Reactions, *Industrial and Engineering Chemistry Research 43*, 6654-6669.

Boelhouwer, J. G., Piepers, H. W., & Drinkenburg, A. A. H. (2001). Particle-Liquid Heat Transfer in Trickle-Bed Reactors. *Chemical Engineering Science 56*, 1181-1187.

Brackbill, J. U., Kothe, D. B., & Zemach, C. (1992). A Continuum Method for Modeling Surface Tension, *Journal of Computational Physics 100*, 335-354.

Cerbelli, S., Garofalo, F., & Giona, M. (2008). Steady-state performance of an infinitely fast reaction in a three-dimensional open Stokes flow. *Chemical Engineering Science 63*, 4396-4411.

FLUENT 6.1. User's Manual to FLUENT 6.1. Fluent Inc. Centrera Resource Park, 10 Cavendish Court, Lebanon, 2005, USA.

GAMBIT 2. User's Manual to GAMBIT 2. Fluent Inc. Centrera Resource Park, 10 Cavendish Court, Lebanon, 2005, USA.

Gladden, L. F., Lim, M. H. M., Mantle, M. D., Sederman, A. J., & Stitt, E. H. (2003). MRI visualisation of two-phase flow in structured supports and trickle-bed reactors. *Catalysis Today 79-80*, 203-210.

Goto, S., & Smith, J. M. (1975). Trickle Bed Reactors Performance: I Hold-up and Mass Transfer Effects. A.I.Ch.E. Journal 21 (1975) 706-713.

Iliuta, I., Larachi, F., Grandjean, B. P. A., & Wild, G. (1999). Gas–Liquid Interfacial Mass Transfer in Trickle-bed Reactors: State-of-the-art Correlations. *Chemical Engineering Science 54* 5633-5645.

Hassanzadeh, H., Abedi, J., & Pooladi-Darvish, M. (2009). A comparative study of flux-limiting methods for numerical simulation of gas–solid reactions with Arrhenius type reaction kinetics. *Computers and Chemical Engineering 33*, 133-143.

Himmelblau, D. M. (1960). Solubilities of Inert Gases in Water. 0°C to Near the Critical Point of Water. *Journal of Chemical Engineering Data 5*, 10-15.

Li, M., & Christofides, P.D. (2008). Optimal control of diffusion-convection-reaction processes using reduced-order models. *Computers and Chemical Engineering 32*, 2123-2135.

Lopes, R. J. G., Silva, A. M. T., & Quinta-Ferreira, R. M. (2007). Screening of Catalysts and Effect of Temperature for Kinetic Degradation Studies of Aromatic Compounds During Wet Oxidation. *Applied Catalysis B: Environmental 73*, 193-202.

Lopes, R.J.G., & Quinta-Ferreira, R.M. (2008). Three-Dimensional Numerical Simulation of Pressure Drop and Liquid Holdup for High-Pressure Trickle-Bed Reactor, *Chemical Engineering Journal 145*, 112-120.

Lopes, R. J. G., & Quinta-Ferreira, R. M. (2009). VOF based Model for Multiphase Flow in High-Pressure Trickle-Bed Reactor: Optimization of Numerical Parameters, *AIChE Journal 55*, 2920-2933.

Lopes, R. J. G., & Quinta-Ferreira, R. M. (2010). Assessment of CFD Euler–Euler method for trickle-bed reactor modelling in the catalytic wet oxidation of phenolic wastewaters, *Chemical Engineering Journal 160*, 293-301.

Nijemeisland, M. & Dixon, A. G. (2001).Comparison of CFD Simulations to Experiment for Convective Heat Transfer in a Gas-Solid Fixed Bed, *Chemical Engineering Science 82*, 231-246.

Piché, S., Larachi, F., Iliuta, I., & Grandjean, B. P. A. (2002). Improving the Prediction of Liquid Back-mixing in Trickle-bed Reactors Using a Neural Network Approach. *Journal of Chemical Technology and Biotechnology 77*, 989-998.

Reid, R. C., Prausnitz, J. M., & Poling, B. E. (1987). The Properties of Gases and Liquids. Mc-Graw-Hill, New York.

Satterfield, C. N., van Eek, M. W., & Bliss, G. S. (1978). Liquid-Solid Mass Transfer in Packed Beds with Downward Concurrent Gas-Liquid Flow. *AIChE Journal 24* (1978) 709-717.

Siddiqi, M. A., & Lucas, K. (1986). Correlations for prediction of diffusion in liquid. *Canadian Journal of Chemical Engineering 64*, 839-843.

Wilke, C. R., & Chang, P. (1955). Correlation of Diffusion Coefficients in Dilute Solutions. *AIChE Journal 1*, 264-269.

Zalc, J.M., & Muzzio, F.J. (1999). Parallel-competitive reactions in a two-dimensional chaotic flow. *Chemical Engineering Science 54*, 1053-1069.

TABLES

Table 1 – Initial and boundary conditions for the gas and liquid phases

	t = 0	*z = 0*
α_G	0.25	0.25
α_L	0.15	0.15
G / (kg/m^2s)	0.1-0.7	0.1-0.7
L / (kg/m^2s)	1-15	1-15
P / bar	30	30
k / (m^2/s^2)	*Eqs 18-20*	
ε / (m^2/s^3)		

Table 2 – Relevant thermophysical properties of gas and liquid phases at P = 30 bar

Properties	Value (P = 30bar) T = 25ºC	T = 200ºC	Units
Liquid phase			
Viscosity	8.925×10^{-4}	1.340×10^{-4}	Pa.s
Density	998.4	866.9	kg/m^3
Surface tension	7.284×10^{-2}	3.770×10^{-2}	N/m
Gas phase			
Viscosity	1.845×10^{-5}	2.584×10^{-5}	Pa.s
Density	35.67	21.97	kg/m^3

Table 3. Dimensionless wall distance parameter (y^+) for the particle surface under different Reynolds numbers

Re		**100**	**500**	**1000**	**1500**	**2500**	**3000**
Coarser mesh (2×10^5 cells)	y^+_{max}	5.12	14.28	24.81	31.07	48.62	53.4
	y^+_{min}	0.01	0.03	0.06	0.08	0.13	0.16
Finer mesh (3×10^6 cells)	y^+_{max}	3.85	9.11	16.73	24.95	42.08	48.91
	y^+_{min}	0.002	0.007	0.008	0.01	0.02	0.03

FIGURE CAPTIONS

Figure 1. Comparison of CFD predictions on normalized Total Organic Carbon conversion for different mesh resolutions (L = 6 kg/m^{2}s, G = 0.3 kg/m^{2}s, P = 30 bar, d_p=2 mm)

Figure 2. Comparison of CFD predictions on normalized bulk temperature for different mesh resolutions (L = 6 kg/m^{2}s, G = 0.3 kg/m^{2}s, P = 30 bar, d_p=2 mm)

Figure 3. Effect of time step on normalized Total Organic Carbon conversion (L = 6 kg/m^{2}s, G = 0.3 kg/m^{2}s, P = 30 bar, d_p=2 mm)

Figure 4. Effect of time step on normalized bulk temperature (L = 6 kg/m^{2}s, G = 0.3 kg/m^{2}s, P = 30 bar, d_p=2 mm)

Figure 5. Convergence plot of mean bulk total organic carbon conversion for various under-relaxation factors: red-0.6, green-0.7, blue-0.8 (L = 6 kg/m^{2}s, G = 0.3 kg/m^{2}s, P = 30 bar, d_p=2 mm)

Figure 6. Convergence plot of mean bulk temperature for various under-relaxation factors: red-0.6, green-0.7, blue-0.8 (L = 6 kg/m^{2}s, G = 0.3 kg/m^{2}s, P = 30 bar, d_p=2 mm

Figure 7. Convergence plot of mean bulk total organic carbon conversion for various mesh sizes: red-1.8×10^6, green-2.2×10^6, blue-2.6×10^6 (L = 6 kg/m^{2}s, G = 0.3 kg/m^{2}s, P = 30 bar, d_p=2 mm

Figure 8. Convergence plot of mean bulk temperature for various mesh sizes: red-1.8×10^6, green-2.2×10^6, blue-2.6×10^6 (L = 6 kg/m^{2}s, G = 0.3 kg/m^{2}s, P = 30 bar, d_p=2 mm

Figure 9. Convergence plot of mean bulk total organic carbon conversion for various time steps: red-10^{-3} s, green-10^{-4} s, blue-10^{-5} s (L = 6 kg/m^{2}s, G = 0.3 kg/m^{2}s, P = 30 bar, d_p=2 mm

Figure 10. Convergence plot of mean bulk temperature for various time steps: red-10^{-3} s, green-10^{-4} s, blue-10^{-5} s (L = 6 kg/m^{2}s, G = 0.3 kg/m^{2}s, P = 30 bar, d_p=2 mm

Figure 11. Instantaneous snapshot of liquid phase distribution colored by total organic carbon concentration (L=6 kg/m^{2}s, G=0.3 kg/m^{2}s, P=30 bar, T=200ºC, d_p=2 mm)

Figure 12. Instantaneous snapshot of liquid phase distribution colored by liquid temperature (L=6 kg/m^{2}s, G=0.3 kg/m^{2}s, P=30 bar, T=200ºC, d_p=2 mm)

FIGURES

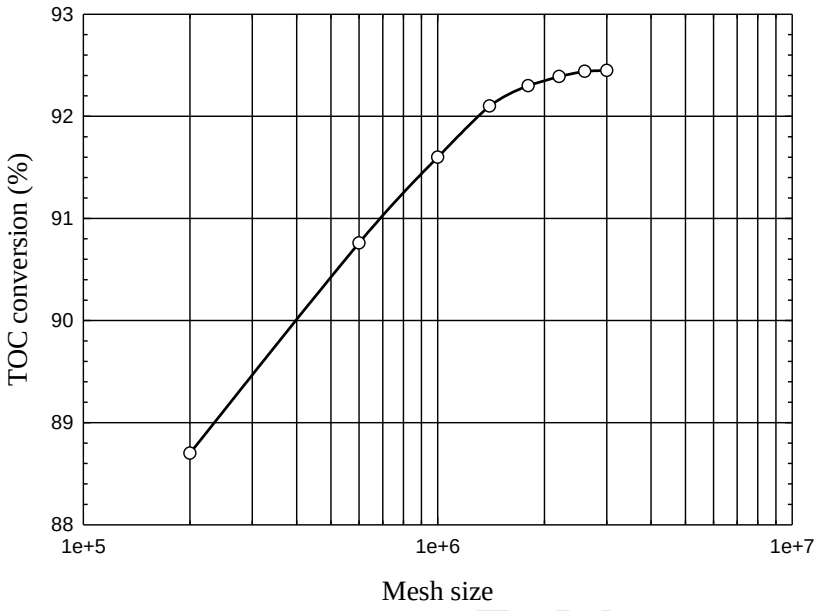

FIGURE 1

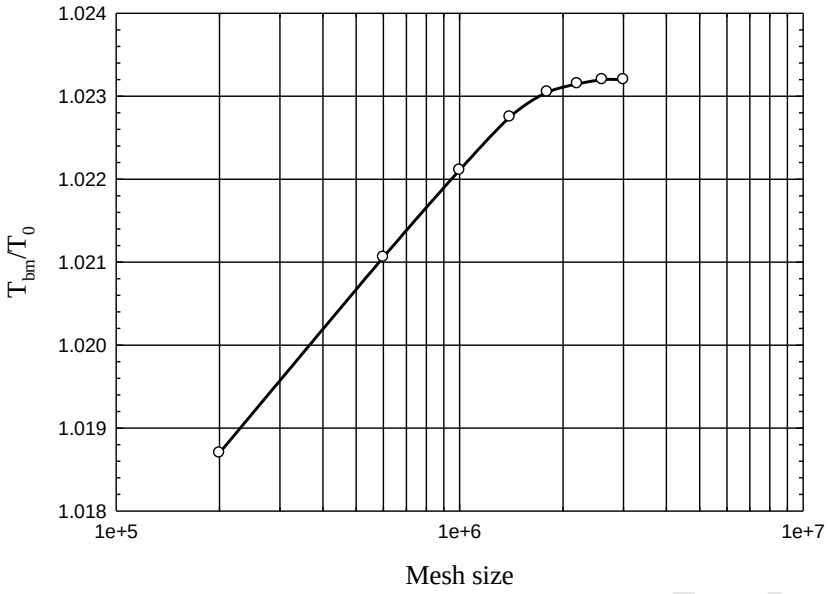

FIGURE 2

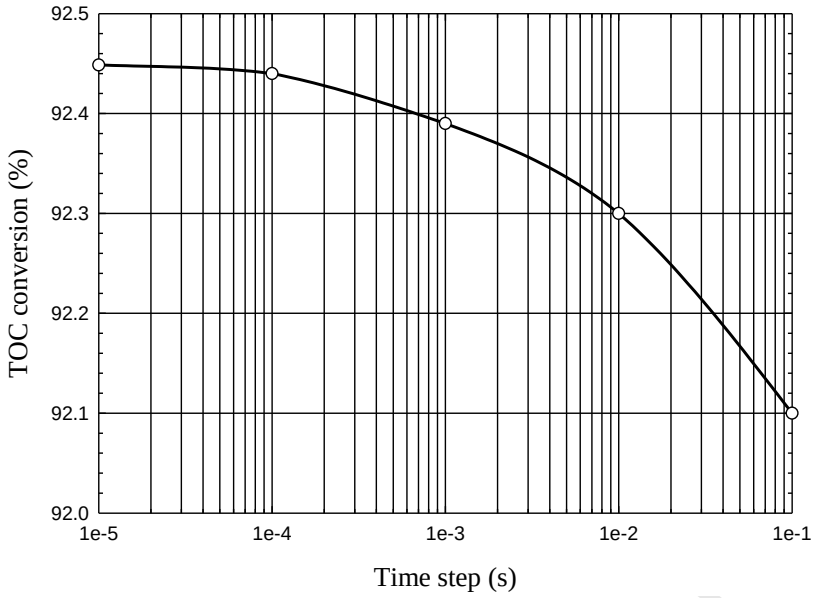

FIGURE 3

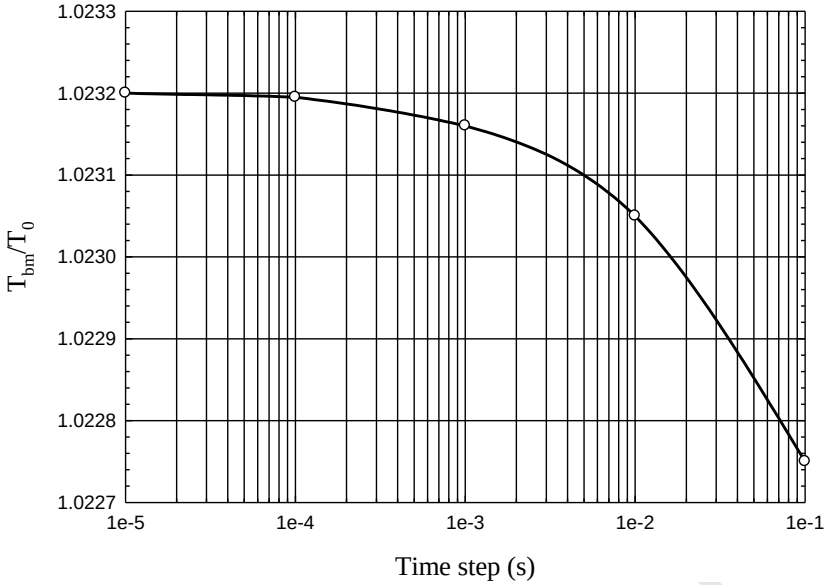

FIGURE 4

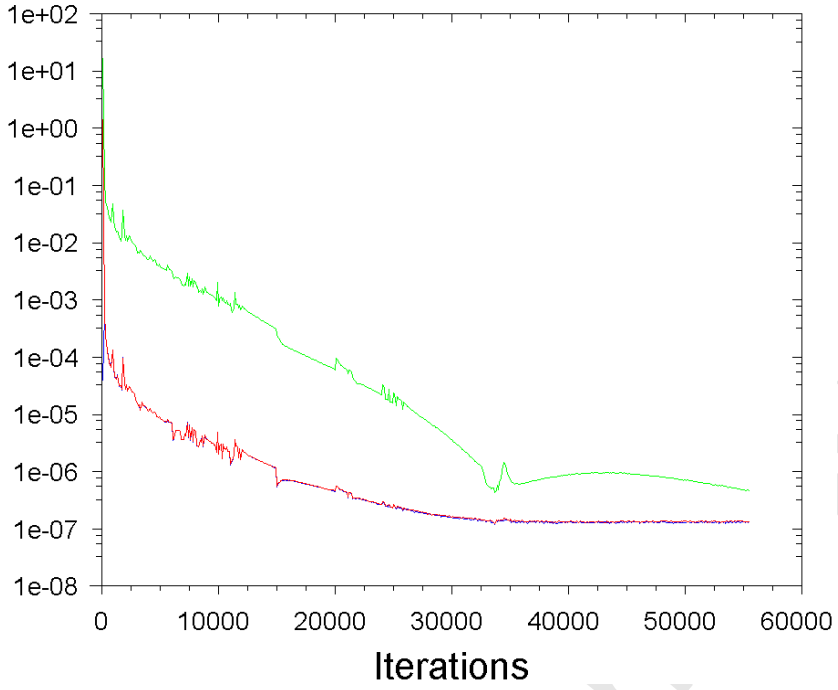

FIGURE 5

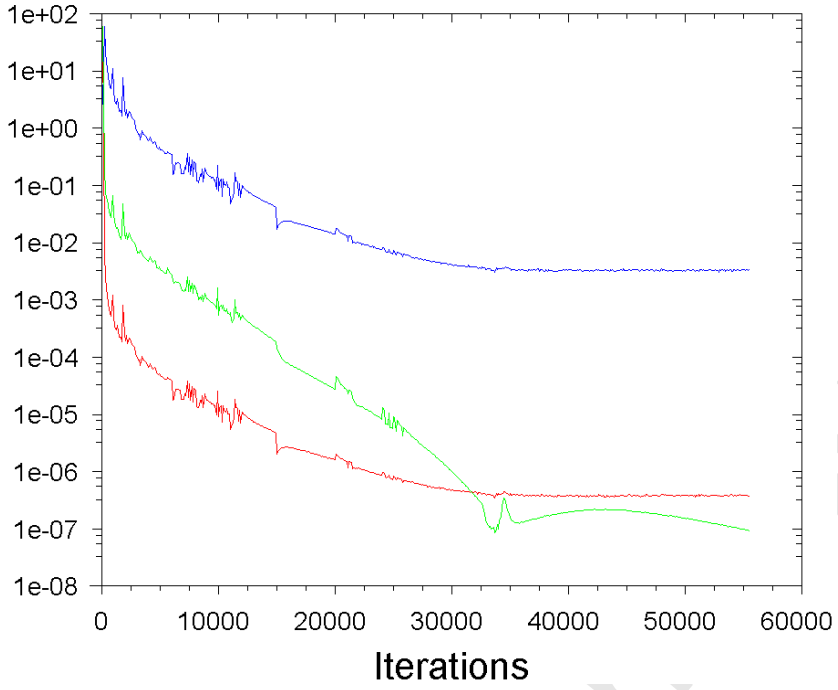

FIGURE 6

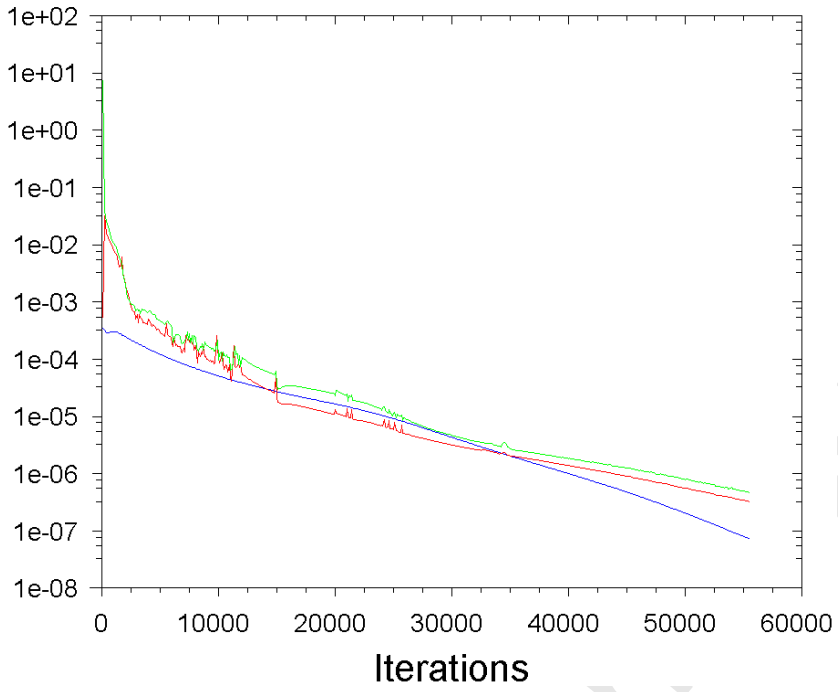

FIGURE 7

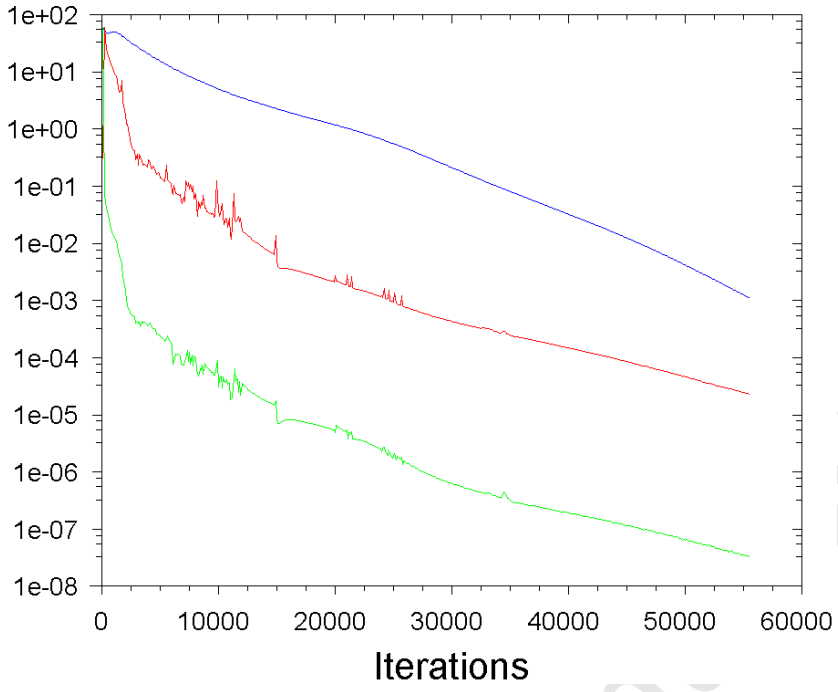

FIGURE 8

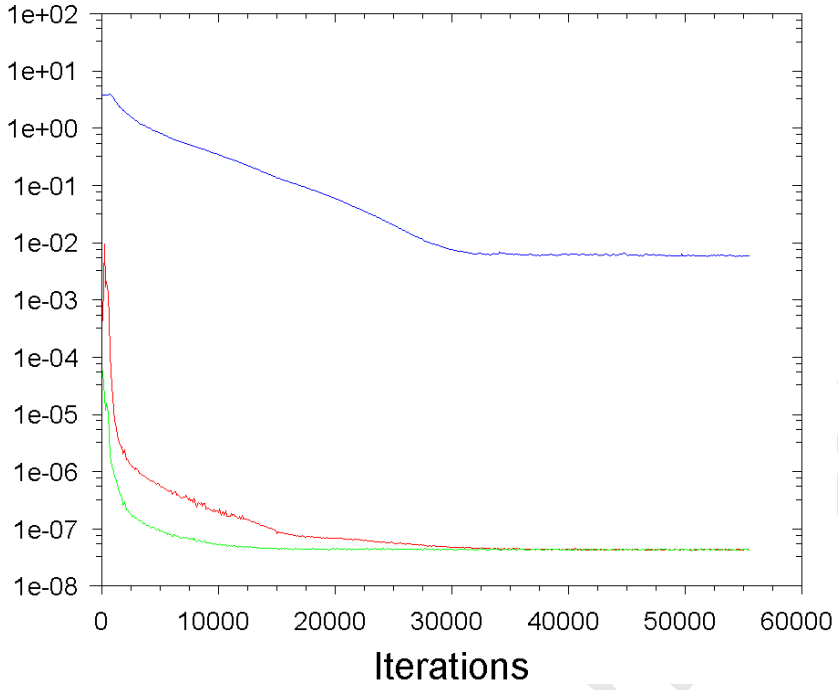

FIGURE 9

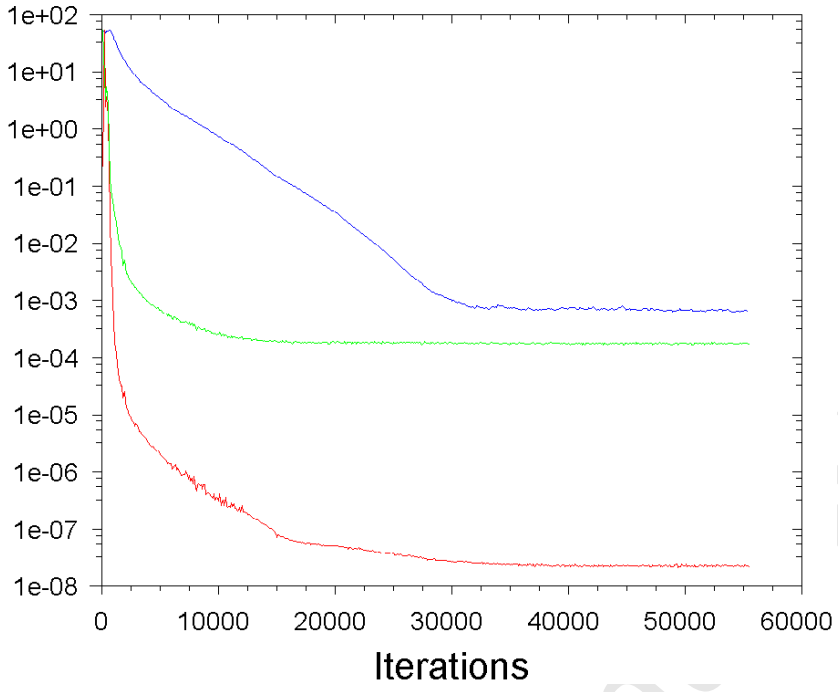

FIGURE 10

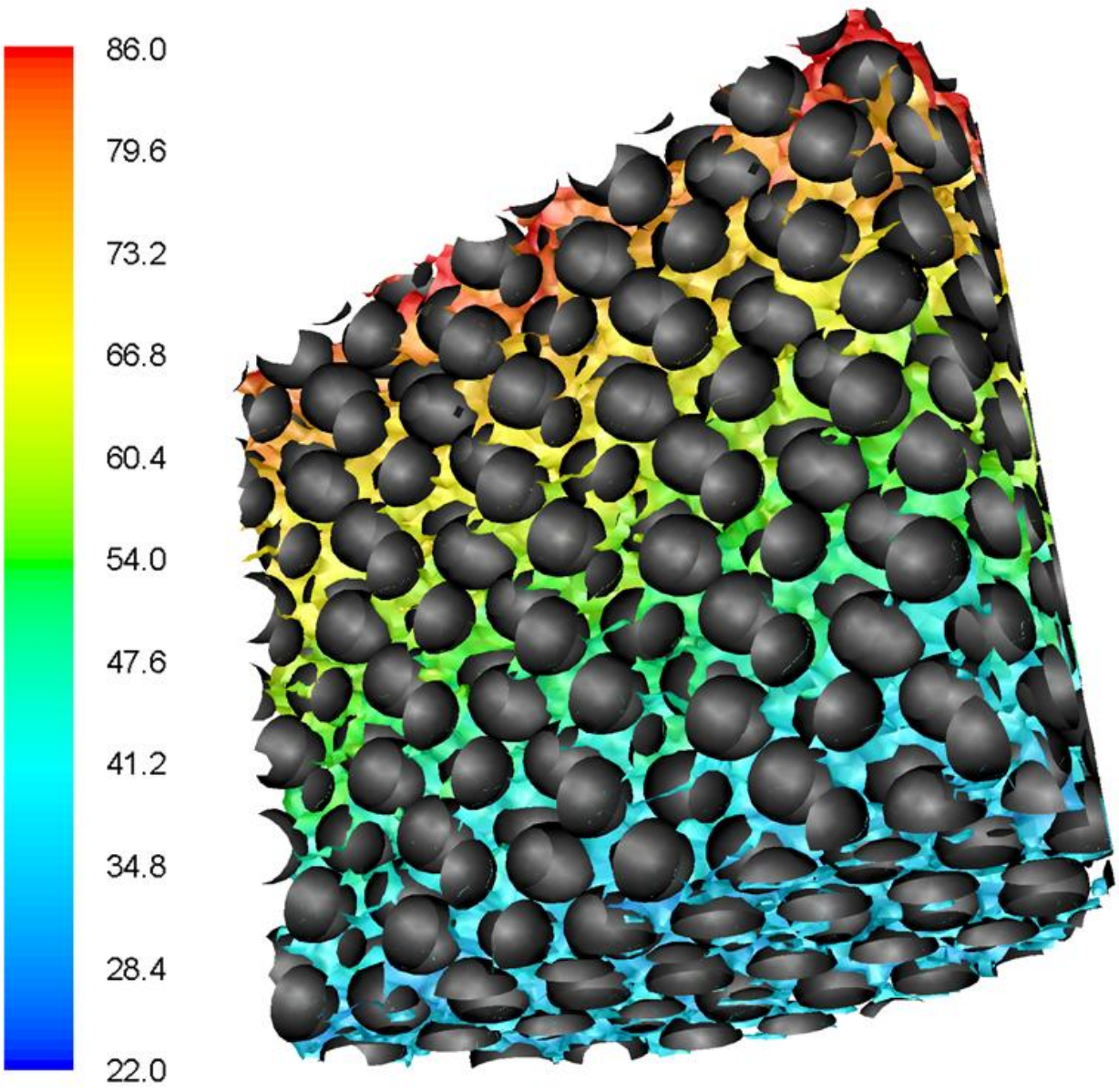

FIGURE 11

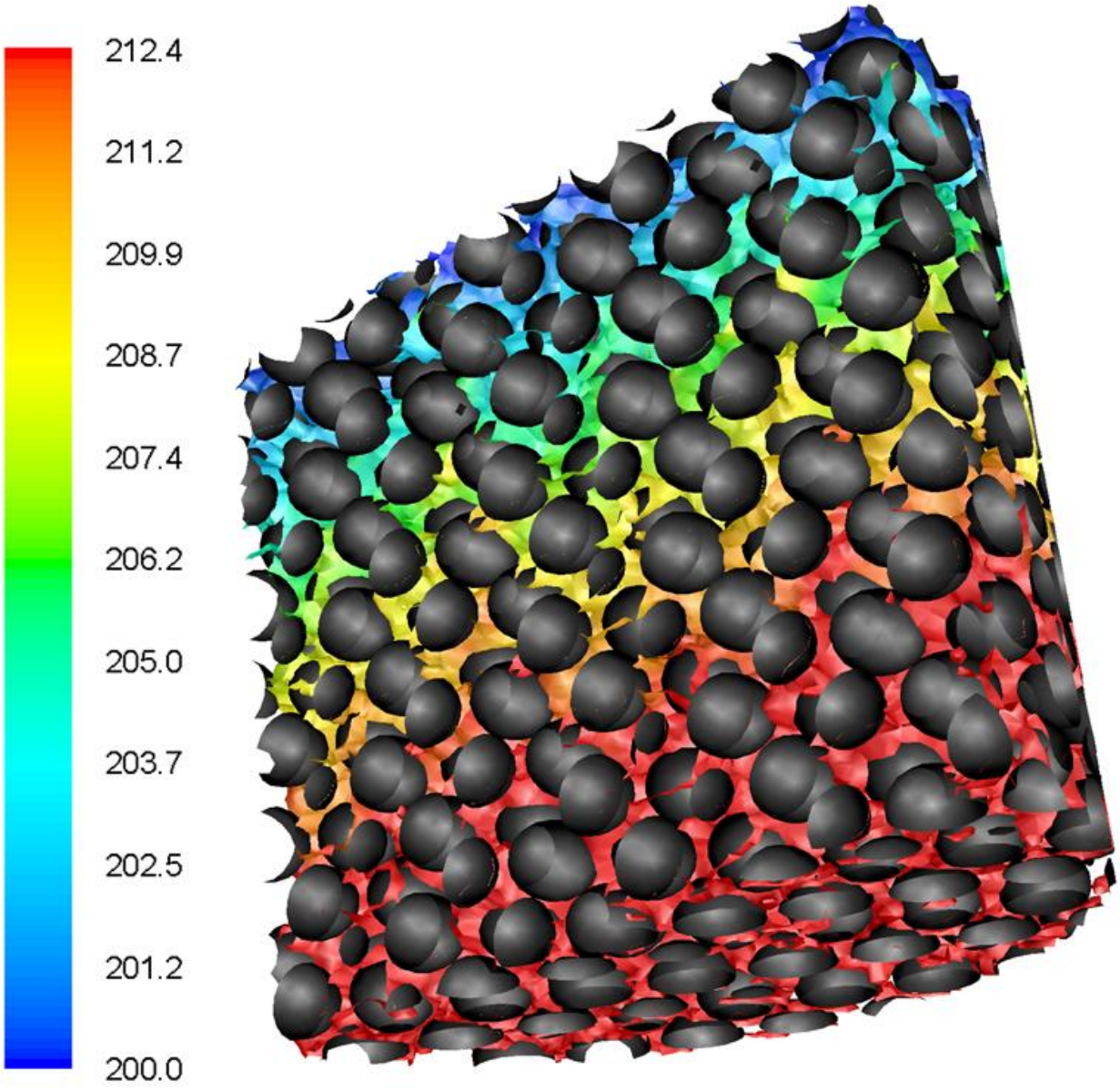

FIGURE 12